Visualization of Phase Evolution in Model Organic Photovoltaic Structures *via* Energy-Filtered Transmission Electron Microscopy

Andrew A. Herzing,†,* Hyun Wook Ro,† Christopher L. Soles,† and Dean M. DeLongchamp†

National Institute of Standards and Technology, Material Measurement Laboratory, 100 Bureau Drive, Gaithersburg, Maryland 20899, United States. †All authors contributed equally.

ABSTRACT

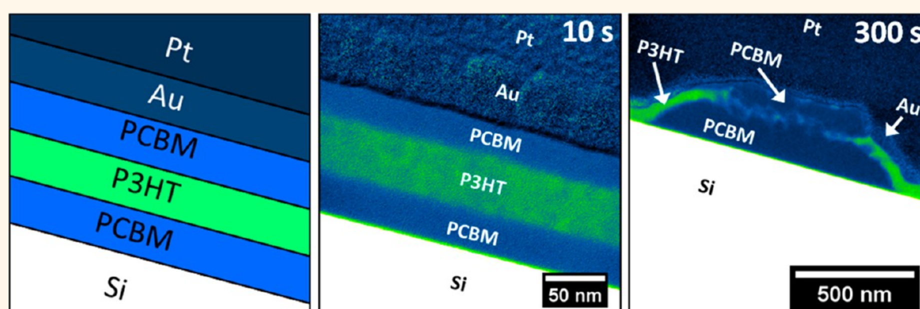

The morphology of the active layer in an organic photovoltaic bulk-heterojunction device is controlled by the extent and nature of phase separation during processing. We have studied the effects of fullerene crystallinity during heat treatment in model structures consisting of a layer of poly(3-hexylthiophene) (P3HT) sandwiched between two layers of [6,6]-phenyl-C_{61}-butyric acid methyl ester (PCBM). Utilizing a combination of focused ion-beam milling and energy-filtered transmission electron microscopy, we monitored the *local* changes in phase distribution as a function of annealing time at 140 °C. In both cases, dissolution of PCBM within the surrounding P3HT was directly visualized and quantitatively described. In the absence of crystalline PCBM, the overall phase distribution remained stable after intermediate annealing times up to 60 s, whereas microscale PCBM aggregates were observed after annealing for 300 s. Aggregate growth proceeded vertically from the substrate interface *via* uptake of PCBM from the surrounding region, resulting in a large PCBM-depleted region in their vicinity. When precrystallized PCBM was present, amorphous PCBM was observed to segregate from the intermediate P3HT layer and ripen the crystalline PCBM underneath, owing to the far lower solubility of crystalline PCBM within P3HT. This process occurred rapidly, with segregation already evident after annealing for 10 s and with uptake of nearly all of the amorphous PCBM by the crystalline layer after 60 s. No microscale aggregates were observed in the precrystallized system, even after annealing for 300 s.

KEYWORDS: TEM · EF-TEM · organic photovoltaics · microanalysis · P3HT · PCBM

The active layer in organic photovoltaic (OPV) devices is typically comprised of a bulk-heterojunction (BHJ) architecture, consisting of an intimate blend of donor and acceptor phases.[1] This type of architecture simultaneously satisfies the requirements for producing a high-efficiency device: (a) domain sizes which are smaller than the excitonic diffusion length (≈10 nm), (b) a large interfacial area to facilitate exciton separation, and (c) a high degree of vertical connectivity to enable charge transport to the surface electrodes.[2] All these morphological features are, in turn, related to the nature and extent of phase separation which occurs during film processing. This process can be altered by, for instance, controlling the solvent evaporation rate[3] or by thermally annealing the film after casting.[4] These parameters are known to alter the morphology of the film as well as the device performance; however, developing a true understanding of this relationship is difficult due to partial crystallization of

* Address correspondence to andrew.herzing@nist.gov.

Received for review June 13, 2013 and accepted August 9, 2013.

Published online August 09, 2013
10.1021/nn402992y

This article not subject to U.S. Copyright. Published 2013 by the American Chemical Society

one or both components during processing, the existence of spatial heterogeneities within the film, and the overall complexity of the BHJ architecture itself.[5] One way of mitigating these complications is to analyze simple model structures and extrapolating the observations to that of a realistic device. Toward this end, a number of groups have recently studied bilayer structures consisting of a layer of poly(3-hexylthiophene) (P3HT) deposited onto a [6,6]-phenyl-C_{61}-butyric acid methyl ester (PCBM) coated substrate.[6−8] In a separate paper,[9] we have reported neutron reflectivity (NR) measurements of a trilayer system composed of a layer of P3HT sandwiched between two layers of PCBM. This approach is very powerful, and has led to important understandings of the mixing behavior as a function of heat treatment conditions. However, NR is restricted to specimens which exhibit no surface roughness above the nanoscale, due to a loss of coherency in the reflected signal. In addition, while NR and other 'bulk' techniques such as dynamic secondary ion-mass spectrometry and X-ray photoelectron spectroscopy provide valuable details regarding the depth distribution of phases within model structures, none of these are sensitive to local compositional variations within the layers themselves as they lack sufficient spatial resolution in the lateral dimensions. To address this gap in the characterization of model OPV systems, we have employed cross-sectional, focused ion-beam (FIB) specimen preparation in concert with energy-filtered transmission electron microscopy (EF-TEM) to directly image the spatial extent of the various phases present as well as their dependence on heat treatment conditions.

Cross-sectional FIB specimen preparation is a technique used to produce electron transparent specimens from specific nanoscale regions of a material.[10] As typically employed, a nearly flat coupon is milled from a bulk specimen using a focused beam of Ga^{+} ions. This coupon is then lifted from the bulk using a micromanipulator, 'microwelded' to a support grid by ion-assisted chemical vapor deposition of a metal, and further thinned with the ion beam until electron transparency has been achieved. Most modern instruments are also equipped with an electron beam column, for imaging during the milling and lift out processes. In the context of OPV research, cross-sectional FIB preparation has proven quite useful for the analysis of full BHJ device stacks in the transmission electron microscopy (TEM),[11−13] since they cannot be analyzed in plan view.

EF-TEM is a spectroscopic imaging technique wherein a postspecimen magnetic prism at the base of the TEM column is used to disperse the transmitted electrons to form an energy-loss spectrum. A slit at the dispersion plane is then used to allow only electrons which have lost a specific amount of energy to pass through to the postslit lenses, which reconstitute the electrons into an image collected by a CCD camera.[14] This technique has shown that subtle changes in the plasmon response of various materials can be used to

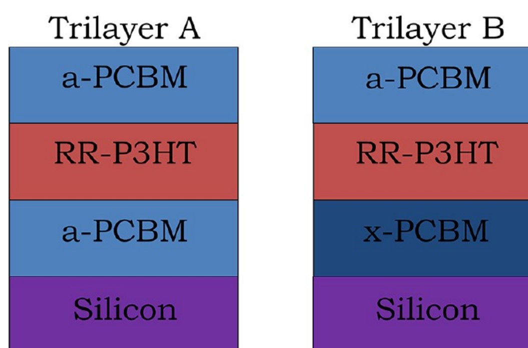

Figure 1. Schematic representation of the two trilayer structures examined in this work.

generate contrast where there is very little present in other imaging modes.[15,16] In our previous work, we have demonstrated that plasmon-loss electrons can be collected in such a way as to produce strong differential contrast between the donor and acceptor phases in OPV films, which is otherwise lacking in conventional bright-field TEM imaging.[17] The technique has subsequently been employed to characterize various OPV systems under a variety of processing conditions.[5,18−20] In addition to plasmon-loss imaging, elemental maps can be formed using EF-TEM by selecting electrons which have lost a specific amount of energy due to inner-shell ionization. Core-loss imaging is a more directly quantifiable approach, since the number of atoms of a particular element in projection at a given image location is proportional to the total energy-loss signal that is collected. Kozub *et al.* employed this approach to collect quantitative maps in P3HT:PCBM films using the sulfur-$L_{2,3}$ and carbon-K edges (located at 164.8 and 283.8 eV, respectively).[21] Since P3HT contains sulfur while PCBM does not, and because PCBM contains a greater concentration of carbon, these maps were then used to measure the phase distribution as a function of heat treatment.

In an effort to understand the effects of PCBM crystallinity on transport and phase behavior during heat treatment, we have used EF-TEM imaging to characterize the series of model trilayer structures that were the subject of our previous paper based on NR characterization.[9] Two trilayer familes were examined (see Figure 1 as well as the Methods section), each consisting of a layer of regioregular (RR)-P3HT sandwiched between two layers of PCBM. In the first case, hereafter referred to as trilayer A, the bottom-most layer of PCBM was in the as-cast state before lamination of the subsequent layers. In contrast, for trilayer B the bottom layer of PCBM was thermally annealed after deposition, such that it was converted to a highly crystalline state prior to lamination of the other layers.

RESULTS AND DISCUSSION

As measured *via* bright-field TEM imaging, the thickness of the cross-sectional FIB specimen prepared from

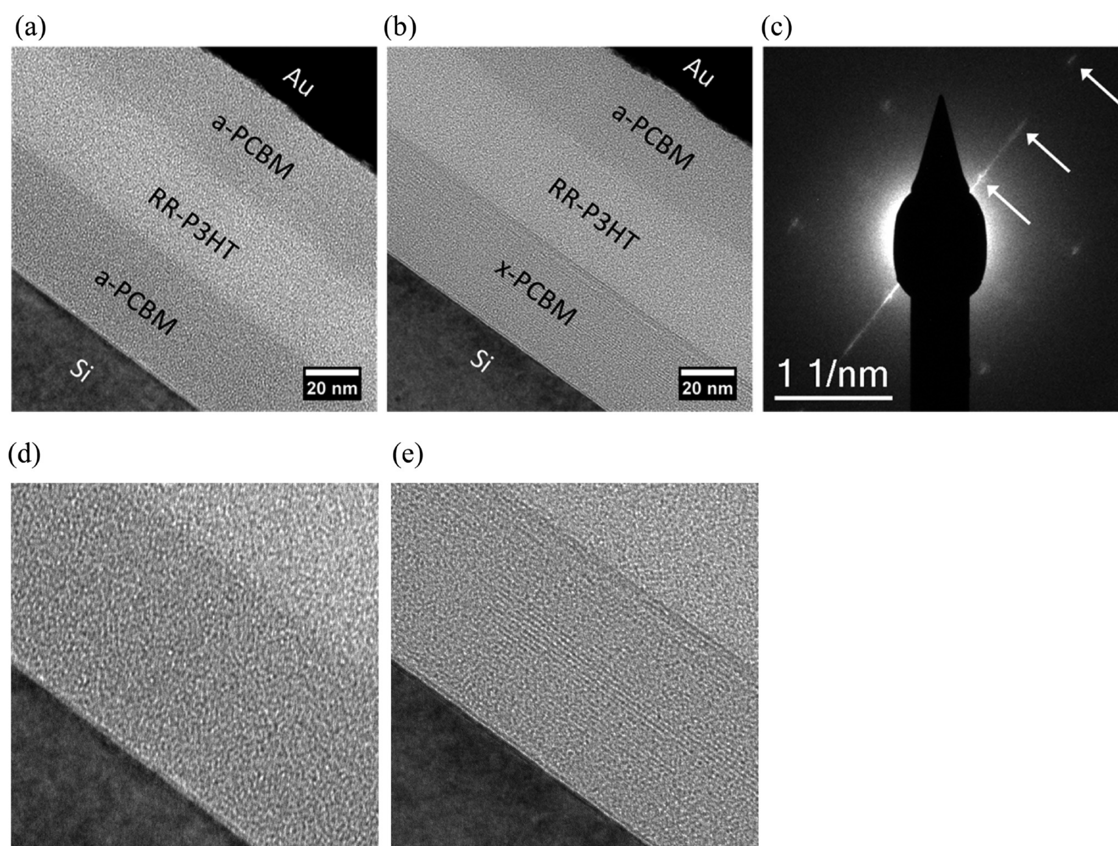

Figure 2. Bright-field TEM images acquired from as-fabricated trilayers A and B (a and b, respectively). Also shown is the SAED pattern from the as-fabricated trilayer B (c) showing crystalline periodicity orthogonal to the film thickness, and 70 nm × 70 nm zoomed images extracted from (a) and (b) detailing the bottom-most PCBM layer in trilayers A and B (d and e, respectively).

each trilayer film compares quite well with the values previously measured *via* NR.[9] This is an important observation, as it indicates that the alteration to the structure of the film by the electron and ion beam during FIB milling was minimal. Further indication of this is shown in high-resolution lattice images collected near the interface of the substrate and the bottom PCBM layer, which show the retained crystalline structure of the Si substrate itself as well as a periodic structure in the crystallized PCBM of trilayer B (Figure 2). FFT analysis of the PCBM region of the TEM images (not shown) reveals two dominant spatial frequencies at 1.14 and 1.85 nm^{-1}. No such periodicity was encountered in the bottom PCBM of trilayer A, or in the top PCBM layer in either system. This confirms that the thermal annealing treatment converted the primary PCBM in trilayer B to a highly crystalline material, and that this periodicity is retained even after the relatively high electron/ion doses imparted during the FIB milling process used to make the thin, cross-sectional specimens.[22]

There is no guarantee that this crystalline structure is indicative of that present in the layer prior to FIB preparation, only that some form of crystallinity has proven resistant to damage. Furthermore, there are regions of the PCBM layer which do not exhibit such fringes, suggesting that the layer is polycrystalline since fringes are only produced from those regions which exhibit the proper orientational relationship with the electron beam to satisfy the Bragg criteria for diffraction. To determine whether the observed crystal structure is consistent with unaltered PCBM and has not been induced *via* exposure to the ion and electron beams during milling, selected-area electron diffraction (SAED) patterns were collected (as shown for the initial trilayer B in the right-most panel of Figure 2). In all samples of the trilayer B family, three reflections were observed, all of which were oriented normal to the film. These were located at 0.64, 1.29, and 1.88 nm^{-1} (indicated by white arrows in the SAED pattern in Figure 2), corresponding to interplanar spacings of 1.56, 0.84, and 0.53 nm. A previous SAED-based study of crystals in thin-films of PCBM reported similar values of 0.84 and 0.52 nm interplanar spacings; nevertheless, no mention was made of a reflection near 1.56 nm.[23] However, similar values have been reported for the one of the unit cell dimensions of crystalline PCBM.[24,25]

The presence of retained PCBM crystallinity was somewhat unexpected. Previous work[22,26] has shown that, due to the low thermal conductivity in most polymer systems, the local temperature increase

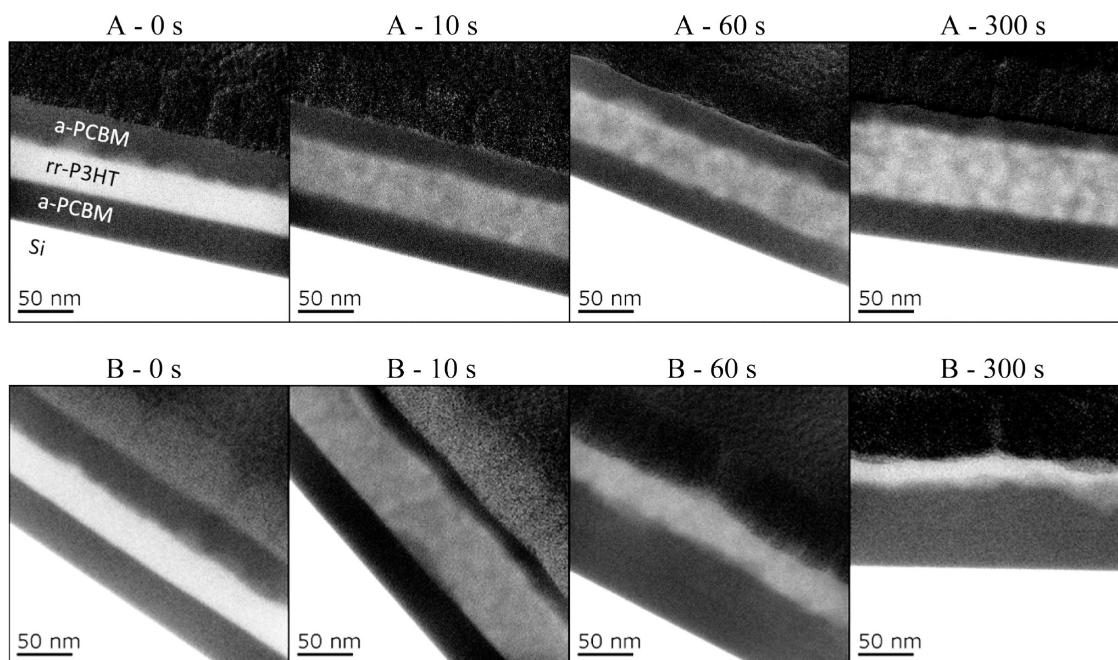

Figure 3. Low-loss EF-TEM ratio images trilayers A and B (top and bottom rows, respectively) as a function of annealing time at 140 °C. From left to right: 0, 10, 60, and 300 s. Bright regions correspond to P3HT, while dark correspond to PCBM.

caused by the ion-beam can be extremely high. According to these authors, the temperature rise (T) can be estimated as

$$T = \frac{P}{\pi a \kappa} \quad (1)$$

where P is the power in the ion beam (probe current multiplied by beam energy), a is the radius of the beam, and κ is the thermal conductivity of the material being milled. Initial thinning was carried out using a 30 keV beam with a probe current of 93 pA, resulting in a nominal probe diameter of 45 nm. If κ is assumed to be 0.1 W/(m K), then the temperature rise is estimated to be approximately 400 K. This value far exceeds the melting temperature of PCBM; however for the final thinning step, a lower energy (5 keV) beam with less current (47 pA) was used. For an estimated probe diameter of 50 nm, this produces a temperature increase of approximately 30 K. Therefore, by using a low intensity final milling procedure in the preparation of cross-sectional specimens, the surface regions altered by previous milling steps using higher intensity beams can be removed and the underlying crystal structure preserved.

The results of low-loss EF-TEM ratio imaging of the two different trilayer structures that were studied as a function of four different annealing times are shown in Figure 3. The intensity in these images is such that, within the organic layers, the brighter regions correspond to P3HT and the darker to PCBM, while the silicon substrate is very intense due to a strong plasmon resonance near 17 eV loss. The as-fabricated structures are quite similar to each other, both in terms of the phase distribution and the thicknesses of each layer, which are close to the expected values (Table 1). It is also important to note that no contrast modulations are observed within the P3HT layer of either system, indicating that the layers exhibit a largely uniform density throughout. Upon annealing for 10 s, the P3HT layer noticeably swelled, and developed small regions of contrast modulation within approximately 10−15 nm in size. Since the contrast mechanism in this imaging mode is dominated by density changes, this suggests that the density is no longer uniform within the P3HT

TABLE 1. Thickness measurements as extracted from low-loss EF-TEM Images of Trilayers A and B after Various Heat Treatment Times at 140 °C[a]

Trilayer A	0 s	10 s	60 s	300 s
total thickness	108 ± 2	111 ± 1	104 ± 4	119 ± 3
bottom PCBM	37 ± 1	34 ± 2	32 ± 2	36 ± 2
RR-P3HT	34 ± 2	46 ± 2	44 ± 5	64 ± 3
top PCBM	36 ± 2	31 ± 1	28 ± 4	19 ± 3

Trilayer B	0 s	10 s	60 s	300 s
total thickness	111 ± 4	117 ± 3	105 ± 8	97 ± 9
bottom PCBM	37 ± 1	38 ± 1	70 ± 3	71 ± 19
RR-P3HT	38 ± 2	62 ± 5	35 ± 7	26 ± 16
top PCBM	36 ± 3	17 ± 3	0	0

[a] All values are in nanometers. Thicknesses given are the mean value of 10 measurements over a lateral film distance of 250−500 nm. Error estimates represent the 95% confidence interval, based on the standard deviation of the mean for each measurement.

layer, by virtue either of localized densification of P3HT or by incorporation of higher density material (*i.e.*, PCBM) within the layer. After annealing for 60 s, the structure of trilayer A remains similar to that observed in the specimen which was annealed for 10 s. It is only after annealing for a full 300 s that further changes in the phase distribution of trilayer A were observed. In this specimen, the degree of swelling of the central P3HT layer has significantly increased along with a decrease in thickness of both the top and bottom layers of PCBM. These results suggest that amorphous PCBM can readily dissolve into the adjacent P3HT layer, and that the amount of PCBM within the P3HT increases with annealing time. It should also be pointed out that, while the layer thicknesses are initially quite homogeneous across the film, roughening of the layer surfaces and interfaces begins after 60 s of annealing, as is evident by the increase in the error of the thickness measurements for each layer and the overall film presented in Table 1. This produces a more heterogeneous nanoscale distribution of PCBM, which only increases at longer annealing times. While bulk techniques such as NR can capture the average distribution over a large area of film, they are not sensitive to finer scale detail such as that which is revealed by EF-TEM analysis, and would result in very poor data if applied to the roughened surface exhibited by the specimens after longer annealing times due to a loss of coherency in the reflected signal.

In contrast to these observations, the structure of trilayer B was found to be altered in much more noticeable ways, even at short annealing times. After annealing for 10 s, the P3HT layer has developed contrast modulations similar to those observed in trilayer A; however, this layer has nearly doubled in thickness along with an accompanying decrease in the thickness of the topmost layer of PCBM. Conversely, the thickness of the bottom-most, crystalline PCBM layer is largely the same as that in the as-fabricated trilayer, indicating that the crystalline PCBM layer is far less soluble than its disordered counterpart. In addition, the presence of the crystalline layer also alters the net flux across the P3HT layer with respect to the case of trilayer A, where the extent of shrinkage in both PCBM layers was nearly the same. These changes are shown more dramatically after 60 s of annealing, after which trilayer B has fully converted to a bilayer structure consisting of a P3HT top layer and an underlayer of PCBM that is twice as thick as the initial layer of crystalline material. It is also notable that the P3HT layer thickness has decreased relative to that in the specimen that was annealed for 10 s, and is now on par with that in the as-fabricated specimen. This suggests that, while the P3HT layer is swollen by PCBM at short annealing times, the net flux across the middle layer is sufficient to allow most of the amorphous PCBM to diffuse across this boundary to combine with the crystalline layer underneath. Further annealing for 300 s only increases the roughness of the two layers and their interfaces while not producing any further alteration of the phase distributions.

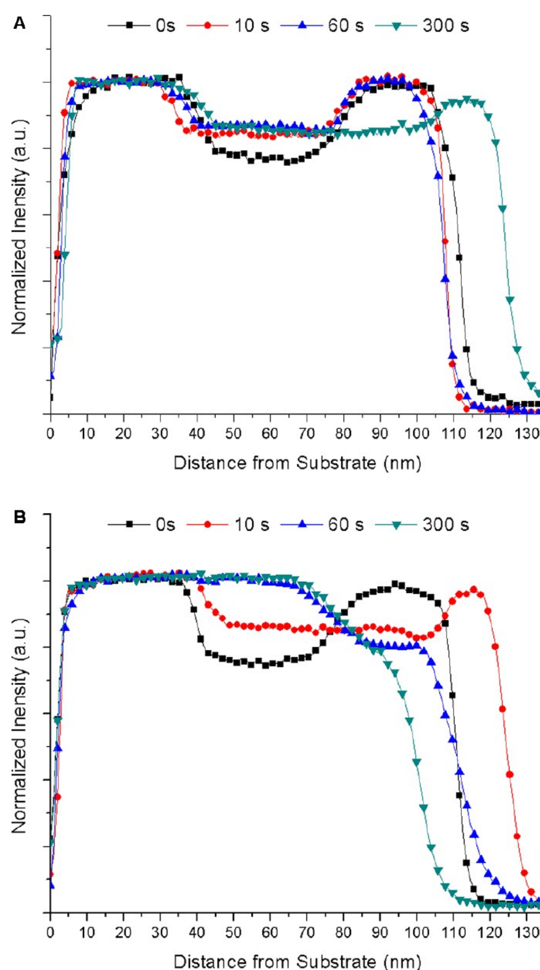

Figure 4. Line profiles extracted along from the carbon K-edge elemental maps along a line perpendicular to the substrate interface from trilayers A and B (top and bottom, respectively). The traces show the relative concentrations of carbon as a function of distance from the silicon substrate. Each profile represents the mean value of 100 pixels at each data point, and the uncertainty in each point is approximately $\pm$3–5% based on the standard deviation of all 100 measurements. For purposes of comparison, the profiles have been normalized to their measured carbon contents near the silicon substrate.

Line plots extracted from the carbon K-edge elemental maps produced *via* core-loss EF-TEM are shown in Figure 4. Since the intensity in these traces is directly proportional to the number of carbon atoms present in the specimen at that point, they can be used to deduce the overall distribution of carbon as a function of heat treatment. For example, the carbon content in the P3HT layer of the initial trilayer A sample is significantly lower than that in the surrounding PCBM layers, as expected based on the nominal densities of P3HT and PCBM (1.1 and 1.6 g cm^{-3}, as measured by Ro *et al.*[9]) and the atom fraction of carbon each contains (40% and 82%, respectively). After annealing at 140 °C, the

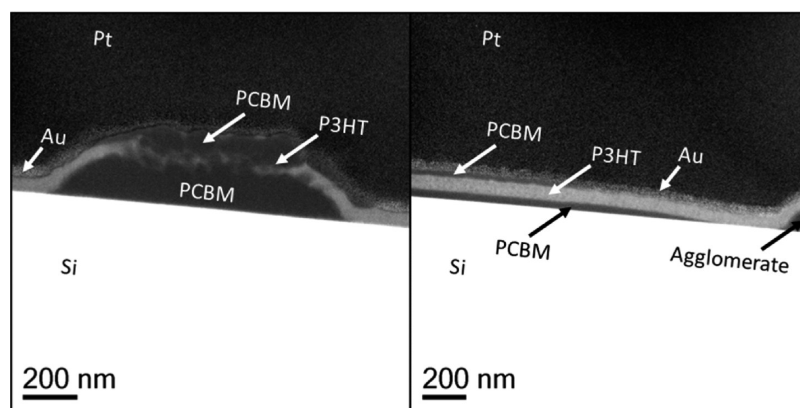

Figure 5. Large-scale aggregate growth in trilayer A after annealing at 140 °C for 300 s. Aggregates (left) were found to exhibit nonuniform composition through their interior with a significant amount of retained P3HT. The aggregates were found to be surrounded by a region of PCBM depletion ≈300 nm wide near the substrate and nearly 1 μm wide near the trilayer surface (right). Beyond this region, the trilayer exhibited the structure depicted previously in the low-loss images acquired from this specimen (see Figure 3).

difference in carbon content between the P3HT layer and the PCBM layers decreases by (6 ± 2) %, confirming the observed uptake of PCBM previously observed *via* low-loss imaging. Within the error of the measurement, no further changes in the carbon content of the P3HT layer were observed after annealing for 60 and 500 s, indicating that the equilibrium PCBM concentration within the P3HT layer is achieved quite rapidly at 140 °C.

For the initial trilayer B specimen, the carbon concentration in the P3HT layer is again much lower than that in PCBM layers. After annealing for 10 s at 140 °C, the difference in carbon content decreased by (10 ± 3)%, similar to the observed difference for trilayer A. However, a slight decrease in the carbon content of the P3HT layer was observed after annealing for 60 s, indicating a net flux into the bottom PCBM layer. These results suggest that the amorphous PCBM component first migrates into the middle P3HT layer and then separates from the P3HT to merge with the crystalline PCBM underneath after longer annealing times. All of these measurements agree quite well with those of the previous NR study,[9] as demonstrated by the plot in Supporting Information Figure S.1 where the layer thicknesses as measured by the C−K edge EF-TEM data is overlaid with those measured *via* NR. Therefore, the EF-TEM analysis confirms the NR data, while also revealing the nanoscale structural features not accessible to NR.

Another feature observed in the case of trilayer A was the presence of large-scale PCBM aggregates after annealing at 140 °C for 300 s. An example of this is shown in Figure 5, where a micrometer-sized aggregate has erupted from the trilayer, exhibiting a height nearly three times that of the original trilayer thickness. The aggregate is surrounded by a PCBM depletion region that is ≈300 nm wide near the substrate, but which extends to nearly 1 μm in width near the trilayer surface. This difference in the extent of PCBM depletion in the top and bottom layers may indicate that the diffusion along the film surface, a pathway not available in the bottom-most layer, is more energetically favored than bulk or interfacial diffusion mechanisms. An alternative explanation is stabilization of the bottom PCBM layer by the presence of the silicon substrate relative to the top layer supported on the middle P3HT. However, further investigation is required to fully illuminate the uptake of the surrounding material by the agglomerates.

Beyond the depleted region, the specimen retains the trilayer structure with a P3HT layer that has swelled considerably, as was shown in Figure 3. However, within ≈300 nm of the aggregate's edge, no contrast fluctuations were observed within the P3HT layer, further suggesting that all PCBM within the vicinity of the macroscale aggregate has been depleted. This is consistent with previous results based on scanning transmission X-ray microscopy by Watt *et al.*,[27] and confirms that all of the surrounding PCBM is swept into the growing aggregate at this annealing temperature.

It is also interesting to note the degree to which the surrounding P3HT layer has accommodated the growth of the PCBM aggregate, the thickness of which under the P3HT has exceeded twice that of the entire starting film thickness. Because of this, the P3HT layer near the perimeter is significantly distorted and pulled upward away from the substrate, no doubt imparting significant strain to the layer. Finally, it is apparent that an irregular, discontinuous region of retained P3HT, which is ≈30 nm thick, is present within the aggregate itself. While retained P3HT content in macroscale PCBM aggregates has been reported *via* Raman spectroscopy,[28,29] to our knowldedge this is the first direct observation of its morphology and location within the aggregate.

Strikingly, SAED analysis of these agglomerates did not reveal any distinct, crystalline peaks, as would be expected for either an agglomerate of nanocrystallites or a single crystal of PCBM and as others have demonstrated for larger PCBM agglomerates.[4,30] As we have seen, it is unlikely that the lack of crystallinity in the

aggregates can be attributed to specimen alteration during the FIB liftout preparation since the crystalline structure of the bottom-most PCBM in trilayer B was retained. While this intriguing result requires further analysis, one possible explanation for the lack of crystallinity in the current aggregates is that the annealing time and/or temperature was insufficient to produce a well-ordered structure, such that the aggregates at this stage are in a 'liquid-like' state with no observable long-range order.

Macroscale aggregates like those observed in trilayer A were not detected in the case of trialyer B. This could be attributed to the limited volume of material analyzed using the FIB-assisted EF-TEM technique; however, optical micrographs acquired from these two samples (Supporting Information Figure S.2) reveal that in fact no appreciable aggregate growth has occurred in trilayer B. Therefore, the presence of a monolithic PCBM crystal layer suppresses the formation of aggregates, and this is likely because the driving force for further growth of the crystal layer is greater than that for the nucleation and growth of additional, smaller crystals. From a practical standpoint, this suggests that nanoscale crystalline PCBM could play a stabilizing role within a BHJ; acting as a controlled sink for the more mobile amorphous PCBM in its vicinity and preventing the macroscale phase separation that so often limits the space of processing parameters available during fabrication. However, this must be balanced against the destabilization of the short-range structure of the film caused by rapid uptake of the nearby amorphous PCBM by the crystalline component.

CONCLUSION

The cross-sectional analysis of model trilayer OPV specimens *via* EF-TEM can be a powerful method for determining the effects of thermal annealing upon the resulting phase distribution. In this study, we have utilized these techniques to investigate the role played by the crystallinity of the fullerene component in the P3HT:PCBM OPV system. In the absence of a crystalline PCBM component, significant uptake of amorphous PCBM into the P3HT was observed; however, the overall phase distribution was otherwise stable. When crystalline PCBM was present in the system, significant migration of amorphous PCBM through the intermediate P3HT was observed, even after short annealing times. At long annealing times, all available amorphous PCBM migrated through the P3HT to bond with the less mobile crystalline PCBM on the other side. Finally, in the absence of crystalline PCBM, macro-scale PCBM aggregate growth was observed, driven by uptake of amorphous PCBM from the surrounding regions of the film. The phenomena revealed by studying model systems in this way allows for a more fundamental understanding of the behavior of these materials, which can then be extrapolated to more complex BHJ device architectures.

METHODS

Materials. For the electon donor phase, regioregular P3HT (Plextronics, Inc.) with a number-average molecular mass of 62 kDa, regioregularity of 99%, and a polydispersity index of 1.9 was utilized. $PC_{61}BM$ (Nano-C, Inc.) was used for the acceptor phase. Both materials were utilized as received.

Trilayer Fabrication. Trilayer films were fabricated by first spin-coating a layer of PCBM from solution (10 mg mL^{-1}, in chloroform) onto a silicon substrate with native oxide surface at ≈523 rad s^{-1} (*i.e.*, 5000 rpm) for 60 s. Next, a P3HT layer was deposited onto the PCBM surface using an elastomer-assisted mechanical lamination process, as described in our previous paper.[9] Briefly, P3HT films were spin-cast onto a OTS-Si substrate, delamintated using a PDMS stamp, and then released onto the previously cast PCBM surface. Finally, the last layer of PCBM was deposited using a similar procedure, also described previously.[9] The PCBM was spin-cast onto a silicon substrate with native oxide surface. Then a PDMS stamp was applied and delaminated by immersing in water. The stamp was then dried using dry nitrogen gas, and the film was mechanically laminated to the awaiting P3HT surface.

Two different trilayers were fabricated in this way. In the first (Trilayer A), the stack was simply built in the sequence just described. In the second (Trilayer B), the first PCBM layer was subjected to a thermal annealing treatment (180 °C for 30 min) prior to lamination of the subsequent layers, resulting in conversion to a crystalline state (as confirmed by GIXD analysis). In summary, both layers are identical with the exception that the first PCBM layer was left in the as-cast state in Trilayer A, while it was converted to a highly crystalline state in Trilayer B.

To study the mixing behavior upon annealing, four different specimens of each of the two trilayer architectures were fabricated. The first was left in the as-fabricated state, while the rest were subjected to thermal annealing treatment at 140 °C for 10, 60, and 300 s, respectively.

Specimen Preparation. Thin, cross-sectional samples of each trilayer were prepared *via* focused ion-beam milling in a dual-beam instrument (FEI Nova NanoLab 600).To minimize specimen damage during the initial stages of this process, each trilayer was first sputter-coated with 25 nm of Au−Pd. A standard TEM liftout protocol was then employed, whereby a 2 μm thick, rectangular coupon was milled from the bulk of the specimen, attached to a Cu support grid, and thinned to electron transparency (<100 nm) using a 30 kV Ga ion beam. Final polishing of the section was carried out using a 5 kV Ga ion beam in order to remove any residual amorphous layer and redeposited material from the surface.

TEM and EF-TEM Analysis. With the use of an FEI 80-300 TEM/STEM instrument equipped with a Gatan Tridiem 865 imaging energy-filter, these thin sections were then imaged using bright-field TEM and energy-filtered imaging. As described in a previous paper, two low-loss images were acquired for 5 s using a 5 eV wide slit centered at 19 and 29 eV loss, or just below and just above the bulk plasmon peak energy at ≈23 eV loss. A 20 μm objective aperture was used for this acquisition, resulting in a collection semiangle of 5 mrads. The ratio of the lower energy-loss image to the higher energy-loss image emphasizes the P3HT-rich regions of the specimen (the PCBM-rich regions could just as easily be displayed by inverting this image). In addition, core-loss elemental maps were acquired using the C−K edge (283.8 eV loss). A standard three-window method was utilized,[31] as implemented in Digital Micrograph (v. 1.83, Gatan, Inc.). Specifically, in this case three images were acquired using a 20 eV wide slit, two centered at energy-loss values below

the edge onset (252 and 272 eV) and a third after the edge-onset (294 eV). In this case, signal-to-noise is enhanced with a smaller collection angle, so a 20 μm objective aperture was employed providing a collection semiangle of 5 mrads. All three images were acquired at full hardware binning (8× or [256 × 256] pixels) and averaged over five acquisitions, each with a 5 s exposure time. The two pre-edge images are used to fit the background signal, assuming a power-law decay, which is then subtracted from the postedge image to form an elemental map.

Conflict of Interest: The authors declare no competing financial interest.

Supporting Information Available: Comparison of layer thicknesses as computed from low-loss EF-TEM and NR. Optical micrographs of trilayers A and B in their initial state and after annealing for 500 s. This material is available free of charge *via* the Internet at http://pubs.acs.org.

Acknowledgment. Certain commercial equipment and materials are identified in this paper in order to specify adequately the experimental procedure. In no case does such identification imply recommendations by the National Institute of Standards and Technology nor does it imply that the material or equipment identified is necessarily the best available for this purpose.

REFERENCES AND NOTES

1. Yu, G.; Gao, J.; Hummelen, J. C.; Heeger, A. J.; Wudl, F. Polymer Photovoltaic Cells: Enhanced Efficiencies *via* a Network of Internal Donor-Acceptor Heterojunctions. *Science* **1995**, *270*, 1789–1791.
2. Dennler, G.; Scharber, M. C.; Brabec, C. J. Polymer-Fullerene Bulk-Heterojunction Solar Cells. *Adv. Mater.* **2009**, *21*, 1323–1338.
3. Li, G.; Shrotriya, V.; Huang, J.; Yao, Y.; Moriarty, T.; Emery, K.; Yang, Y. High-Efficiency Solution Processable Polymer Photovoltaic Cells by Self-Organization of Polymer Blends. *Nat. Mater.* **2005**, *4*, 864–868.
4. Verploegen, E.; Mondal, R.; Bettinger, C. J.; Sok, S.; Toney, M. F.; Bao, Z. Effects of Thermal Annealing Upon the Morphology of Polymer-Fullerene Blends. *Adv.Funct. Mater.* **2010**, *20*, 3519–3529.
5. DeLongchamp, D. M.; Kline, R. J.; Herzing, A. Nanoscale Structure Measurements for Polymer-Fullerene Photovoltaics. *Energy Environ. Sci.* **2012**, *5*, 5980–5993.
6. Collins, B. A.; Gann, E.; Guignard, L.; He, X.; McNeill, C. R.; Ade, H. Molecular Miscibility of Polymer-Fullerene Blends. *J. Phys. Chem. Lett.* **2010**, *1*, 3160–3166.
7. Chen, D.; Liu, F.; Wang, C.; Nakahara, A.; Russell, T. P. Bulk Heterojunction Photovoltaic Active Layers *via* Bilayer Interdiffusion. *Nano Lett.* **2011**, *11*, 2071–2078.
8. Treat, N. D.; Brady, M. A.; Smith, G.; Toney, M. F.; Kramer, E. J.; Hawker, C. J.; Chabinyc, M. L. Interdiffusion of PCBM and P3HT Reveals Miscibility in a Photovoltaically Active Blend. *Adv. Energy Mater.* **2011**, *1*, 82–89.
9. Ro, H. W.; Akgun, B.; O'Connor, B. T.; Hammond, M.; Kline, R. J.; Snyder, C. R.; Satija, S. K.; Ayzner, A. L.; Toney, M. F.; Soles, C. L.; *et al.* Poly(3-hexylthiophene) and [6, 6]-Phenyl-C_{61}-butyric Acid Methyl Ester Mixing in Organic Solar Cells. *Macromolecules* **2012**, *45*, 6587–6599.
10. Giannuzzi, L.; Stevie, F. A Review of Focused Ion Beam Milling Techniques for TEM Specimen Preparation. *Micron* **1999**, *30*, 197–204.
11. Chen, D.; Nakahara, A.; Wei, D.; Nordlund, D.; Russell, T. P. P3HT/PCBM Bulk Heterojunction Organic Photovoltaics: Correlating Efficiency and Morphology. *Nano Lett.* **2010**, *11*, 561–567.
12. Heeger, A. J.; Moon, J. S.; Lee, J. K.; Cho, S.; Byun, J. Columnlike" Structure of the Cross-Sectional Morphology of Bulk Heterojunction Materials. *Nano Lett.* **2009**, *9*, 230–234.
13. Loos, J.; van Duren, J. K. J.; Morrissey, F.; Janssen, R. A. J. The Use of the Focused Ion Beam Technique to Prepare Cross-Sectional Transmission Electron Microscopy Specimen of Polymer Solar Cells Deposited on Glass. *Polymer* **2002**, *43*, 7493–7496.
14. Grogger, W.; Varela, M.; Ristau, R.; Schaffer, B.; Hofer, F.; Krishnan, K. M. Energy-Filtering Transmission Electron Microscopy on the Nanometer Length Scale. *J. Electron Spectrosc. Relat. Phenom.* **2005**, *143*, 139–147.
15. Daniels, H. R.; Brydson, R.; Brown, A.; Rand, B. Quantitative Valence Plasmon Mapping in the TEM: Viewing Physical Properties at the Nanoscale. *Ultramicroscopy* **2003**, *96*, 547–558.
16. Gass, M. H.; Koziol, K. K. K.; Windle, A. H.; Midgley, P. A. Four-Dimensional Spectral Tomography of Carbonaceous Nanocomposites. *Nano Lett.* **2006**, *6*, 376–379.
17. Herzing, A. A.; Richter, L. J.; Anderson, I. M. 3D Nanoscale Characterization of Thin-Film Organic Photovoltaic Device Structures *via* Spectroscopic Contrast in the TEM. *J. Phys. Chem. C* **2010**, *114*, 17501–17508.
18. Hammond, M. R.; Kline, R. J.; Herzing, A. A.; Richter, L. J.; Germack, D. S.; Ro, H. W.; Soles, C. L.; Fischer, D. A.; Xu, T.; Yu, L.; *et al.* Molecular Order in High-Efficiency Polymer/Fullerene Bulk Heterojunction Solar Cells. *ACS Nano* **2011**, *5*, 8248–8257.
19. Clarke, T. M.; Rodovsky, D. B.; Herzing, A. A.; Peet, J.; Dennler, G.; DeLongchamp, D.; Lungenschmied, C.; Mozer, A. J. Significantly Reduced Bimolecular Recombination in a Novel Silole-Based Polymer: Fullerene Blend. *Adv. Energy Mater.* **2011**, *1*, 1062–1067.
20. Drummy, L. F.; Davis, R. J.; Moore, D. L.; Durstock, M.; Vaia, R. a.; Hsu, J. W. P. Molecular-Scale and Nanoscale Morphology of P3HT:PCBM Bulk Heterojunctions: Energy-Filtered TEM and Low-Dose HREM. *Chem. Mater.* **2011**, *23*, 907–912.
21. Kozub, D. R.; Vakhshouri, K.; Orme, L. M.; Wang, C.; Hexemer, A.; Gomez, E. D. Polymer Crystallization of Partially Miscible Polythiophene/Fullerene Mixtures Controls Morphology. *Macromolecules* **2011**, 5722–5726.
22. Bassim, N.; Gregorio, B. DE; Kilcoyne, A.; Scott, K.; Chou, T.; Wirick, S.; Cody, G.; Stroud, R. Minimizing Damage During FIB Sample Preparation of Soft Materials. *J. Microsc.* **2012**, *245*, 288–301.
23. Yang, X.; VanDuren, J. K. J.; Rispens, M. T.; Hummelen, J. C.; Janssen, R. A. J.; Michels, M. A. J.; Loos, J. Crystalline Organization of a Methanofullerene as Used for Plastic Solar-Cell Applications. *Adv. Mater.* **2004**, *16*, 802–806.
24. Li, L.; Lu, G.; Li, S.; Tang, H.; Yang, X. Epitaxy-Assisted Creation of PCBM Nanocrystals and Its Application in Constructing Optimized Morphology for Bulk-Heterojunction Polymer Solar Cells. *J. Phys. Chem. B* **2008**, *112*, 15651–15658.
25. Rispens, M. T.; Meetsma, A.; Rittberger, R.; Brabec, C. J.; Sariciftci, N. S.; Hummelen, J. C. Influence of the Solvent on the Crystal Structure of PCBM and the Efficiency of MDMO-PPV: PCBM "plastic"solar Cells. *Chem. Commun.* **2003**, 2116–2118.
26. Kim, S.; Jeong Park, M.; Balsara, N. P.; Liu, G.; Minor, A. M. Minimization of Focused Ion Beam Damage in Nanostructured Polymer Thin Films. *Ultramicroscopy* **2010**, *111*, 191–199.
27. Watts, B.; Belcher, W. J.; Thomsen, L.; Ade, H.; Dastoor, P. C. A Quantitative Study of PCBM Diffusion During Annealing of P3HT:PCBM Blend Films. *Macromolecules* **2009**, *42*, 8392–8397.
28. Wang, X.; Zhang, D.; Braun, K.; Egelhaaf, H.-J.; Brabec, C. J.; Meixner, A. J. High-Resolution Spectroscopic Mapping of the Chemical Contrast from Nanometer Domains in P3HT: PCBM Organic Blend Films for Solar-Cell Applications. *Adv. Funct. Mater.* **2009**, *20*, 492–499.
29. Klimov, E.; Li, W.; Yang, X.; Hoffmann, G.; Loos, J. Scanning Near-Field and Confocal Raman Microscopic Investigation of P3HT-PCBM Systems for Solar Cell Applications. *Macromolecules* **2006**, *39*, 4493–4496.
30. He, C.; Germack, D. S.; Joseph Kline, R.; DeLongchamp, D. M.; Fischer, D. a.; Snyder, C. R.; Toney, M. F.; Kushmerick, J. G.; Richter, L. J. Influence of Substrate on Crystallization in Polythiophene/Fullerene Blends. *Sol. Energy Mater. Sol. Cells* **2011**, 1–7.
31. Egerton, R. F. *Electron Energy-loss Spectroscopy in the Electron Microscope*; 2nd ed.; Plenum Press: New York, 1996; pp 321−324.